RSC Advances

PAPER

View Article Online
View Journal | View Issue

Cite this: *RSC Adv.*, 2024, **14**, 23177

Lead-free iron-doped $Cs_3Bi_2Br_9$ perovskite with tunable properties†

Thiri Htun,[a] Amr Elattar,[bc] Hytham Elbohy,[d] Kosei Tsutsumi,[a] Kazumasa Horigane,[e] Chiyu Nakano,[f] Xiaoyu Gu,[g] Hiroo Suzuki,[a] Takeshi Nishikawa,[a] Aung Ko Ko Kyaw *[g] and Yasuhiko Hayashi*[a]

Received 3rd June 2024
Accepted 9th July 2024

DOI: 10.1039/d4ra04062g

rsc.li/rsc-advances

Perovskite based on cesium bismuth bromide offers a compelling, non-toxic alternative to lead-containing counterparts in optoelectronic applications. However, its widespread usage is hindered by its wide bandgap. This study investigates a significant bandgap tunability achieved by introducing Fe doping into the inorganic, lead-free, non-toxic, and stable $Cs_3Bi_2Br_9$ perovskite at varying concentrations. The materials were synthesized using a facile method, with the aim of tuning the optoelectronic properties of the perovskite materials. Characterization through techniques such as X-ray diffraction, Raman spectroscopy, X-ray photoelectron spectroscopy, energy dispersive spectroscopy (EDS), and UV-vis spectroscopy was conducted to elucidate the transformation mechanism of the doping materials. The substitution process results in a significant change in the bandgap energy, transforming from the pristine $Cs_3Bi_2Br_9$ with a bandgap of 2.54 eV to 1.78 eV upon 70% Fe doping. The addition of 50% Fe in $Cs_3Bi_2Br_9$ leads to the formation of the orthorhombic structure in $Cs_2(Bi,Fe)Br_5$ perovskite, while complete Fe alloying at 100% results in the phase formation of $CsFeBr_4$ perovskite. Our findings on regulation of bandgap energy and crystal structure through B site substitution hold significant promise for applications in optoelectronics.

Introduction

In recent years, lead-based halide perovskites with the formula ABX_3, where A is a cation (*e.g.*, methylammonium, MA^+, formamidinium, FA^+, cesium, Cs^+), B is lead (Pb^{2+}), and X is the halogen (*e.g.*, I^-, Br^-, and Cl^-), has gained widespread use in ubiquitous optoelectronic devices including photovoltaics, light-emitting diode, laser and photodetector due to their excellent optical and electrical properties.[1–7] These perovskites can be divided into two categories: organic–inorganic perovskites and all-inorganic perovskites, depending on the A cation.[3] Organic cations are prone to decomposition compared to inorganic cations.[2] Moreover, the toxicity and the moisture sensitivity of lead, a component in these perovskites, limit their stability for certain applications.[8–11] Therefore, multiple attempts have been made to substitute lead ions with other metal ions exhibiting similar electronic configurations, such as Sn^{2+}, Ge^{2+}, Bi^{3+}, and Sb^{3+}, aiming for eco-friendly and stable perovskites.[12,13] While tin-based perovskites present lower toxicity and a narrower bandgap than their lead-based counterparts, their susceptibility to moisture and oxygen due to rapid oxidation from Sn^{2+} to Sn^{4+} poses challenges. Germanium-based perovskites share similar stability and electronic and optical properties with lead-based perovskites, but their high cost and spontaneous oxidation during the fabrication process hinder practical applications.[8,14] Alternatively, double perovskites with the general formula $A_2M^+M^{3+}X_6$ have been synthesized by changing the ABX_3 structure, replacing Pb^{2+} with one monovalent cation, M^+ (*e.g.*, Cu^+, Ag^+, Au^+, In^+) and one trivalent cation, M^{3+} (*e.g.*, Bi^{3+}, Sb^{3+}). This innovation results in Pb-free quaternary materials, representing a significant advancement with enhanced functionalities, particularly in solar absorbers.[15–17] Another popular perovskite structure, $A_3B_2X_9$, characterized by a monovalent cation A (Na^+, K^+, Rb^+, Cs^+, and $CH_3NH_3^+$), a trivalent cations B (Bi^{3+} and Sb^{3+}), and a halogen atom X, has recently garnered increased interest in solar cells and photonic applications.[8,18–21]

Within the $A_3B_2X_9$ perovskite structure, diverse crystal structures exist, classified as 0D, 1D, and 2D depending on the B–X sublattice. The zero-dimensional (0D) structure have a hexagonal structure, in which A_3X_9 units are ordered with B

---

[a] *Graduate School of Natural Science and Technology, Okayama University, Japan. E-mail: hayashi.yasuhiko@ec.okayama-u.ac.jp*

[b] *Department of Chemistry, Faculty of Science, Ain Shams University, Cairo, Egypt*

[c] *Industrial & Manufacturing Engineering, FAMU-FSU College of Engineering, 2525 Pottsdamer St, Tallahassee, Florida, 32310, USA*

[d] *Physics Department, Faculty of Science, Damietta University, Egypt*

[e] *Research Institute for Interdisciplinary Science, Okayama University, Japan*

[f] *Advanced Science Research Center, Okayama University, Okayama, Japan*

[g] *Guangdong University Key Laboratory for Advanced Quantum Dot Displays and Lighting and Department of Electronic & Electrical Engineering, Southern University of Science and Technology, P. R. China. E-mail: aung@sustech.edu.cn*

† Electronic supplementary information (ESI) available. See DOI: https://doi.org/10.1039/d4ra04062g

cations in octahedral interstitial sites, resulting in isolated $[B_2X_9]^{3-}$ dimers. In a one-dimensional structure (1D), double chains form based on corner-sharing $[BX_6]^{3-}$ octahedra. The two-dimensional (2D) structure, where the layers are corrugated like corner-connected $[BX_6]^{3-}$ octahedra, is the most similar to the cubic perovskite that appeared by removing the third B site cation from cubic ABX_3. The 2D structure has a narrow bandgap, superior defect tolerance, higher electron and hole mobility, and excellent stability compared to the 0D and 1D structures. Therefore, it plays a crucial role in controlling the bandgap and enhancing optical absorption in lead-free perovskite materials.[22,23]

Bismuth-based perovskites ($A_3Bi_2X_9$) emerge as attractive alternatives due to their non-toxicity, desirable moisture and air stability,[24] and excelle nt water stability. Bi^{3+} shares a similar electronic configuration and ionic radius with Pb^{2+}, making it a viable substitute.[14,25–30] All inorganic Bi^{3+}-based perovskites have obtained increased attention in various optoelectronic applications owing to their superior stability and low toxicity.[31–33] Various Bi^{3+} based perovskites, including Cs_3BiBr_6, $CsBi_3I_{10}$, $Cs_3Bi_2Br_9$, $Cs_2AgBiBr_6$ and $Cs_3Bi_2I_9$, have been successfully synthesized.[34] Among these, all-inorganic Bi-based perovskites using Cs as A cation exhibit enhanced crystallinity and superior optoelectronic properties compared to organic–inorganic counterparts.[2] The choice of Cs as the cation contributes to improve structure stability and overall performance of perovskite materials.[35–37] Doping strategies can further be employed on pristine perovskite material to fine-tune their optical and electronic properties. Siqi Dai *et al.* investigated the effect of Sb doping on pristine $Cs_3Bi_2Br_9$ perovskite, finding that it reduced the bandgap from 2.59 eV to 2.22 eV. The mixed alloy occupied a smaller bandgap than both the Bi-based and Sb-based perovskites.[38] Amr Elattar *et al.* demonstrated that doping of Cu in $Cs_3Bi_2Br_9$ perovskite significantly reduces the bandgap from 2.56 eV for pristine $Cs_3Bi_2Br_9$ to 1.77 eV at 100% Cu.[23] Mrinmoy Roy *et al.* studied the effect of Pb substitution in $Cs_3Bi_2Br_9$ layered perovskites, finding that the bandgap is reduced from 2.62 eV to 2.23 eV due to the emergence of defect states between the bands.[39] Fuxiang *et al.* investigated the impact of Fe doping in the double perovskite $Cs_2AgInxFe_{1-x}Cl_6$, observing a notable reduction in bandgap from 2.8 eV in the pristine material to 1.6 eV in the Fe-doped variants. This highlights the effectiveness of Fe in substantially reducing the bandgap of perovskite materials.[40] Moreover, iron, being the most abundant element on Earth's surface, offers a non-toxic, environmentally friendly, and cost-effective option.[41–44]

Herein, we incorporated Fe ions into the bismuth-based ($Cs_3Bi_2Br_9$) perovskite, effectively modulating the bandgap of $Cs_3Bi_{2-x}Fe_xBr_9$ over a wide range, from 2.54 eV to 1.78 eV. Furthermore, we investigated the impact of Fe doping on the pristine $Cs_3Bi_2Br_9$ perovskite. The substitution of Fe^{3+} for Bi^{3+} in the matrix, resulted in the formation of a secondary phase ($Cs_2(Bi,Fe)Br_5$) and a ternary phase ($CsFeBr_4$) with varying proportions of alloying elements. The incorporation of Fe^{3+} enables the fine-tuning of the optical properties of the doped materials, paving the way for potential applications in optoelectronic devices.

Materials and methods

Materials

In our experimental procedure, we added cesium bromide (CsBr, 98%), bismuth III bromide ($BiBr_3$, 99%), and iron III bromide ($FeBr_3$, anhydrous) to an 8 ml volume of hydrobromic acid (HBr). It is worth noting that all chemicals were used without further purification.

Synthesis of perovskite crystals

We prepared $Cs_3Bi_2Br_9$ with varying Fe doping concentrations (0, 5, 20, 50, 70, and 100 at%). This was achieved by combining 3 mmol of CsBr, $2 - x$ mmol of $BiBr_3$, and x mmol of $FeBr_3$ into 8 ml of hydrobromic acid (HBr), as shown in Table 1. The mixture was then subjected to heating at 150 °C for 48 h, followed by a gradual cooling to room temperature at a rate of 10 ° C day^{-1}. This controlled thermal treatment resulted in the successful formation of Fe-doped $Cs_3Bi_2Br_9$ perovskite crystals.

Characterization

In our analysis, we employed a scanning electron microscope (SEM), specifically the JEOL JEM-2100F model, operating at 12 kV. To gain insights into the morphology and elemental composition of the samples, energy dispersive spectroscopy (EDS) was utilized. Elemental analysis was conducted using the SEM with EDS capabilities. For structural characterization, powder X-ray diffraction (XRD) data were collected at room temperature. A conventional diffractometer, specifically the Rigaku RINT-TTR III, with Bragg–Brentano geometry and a Cu-Kαradiation source ($\lambda = 1.5418$ Å), was utilized. The obtained diffraction data were analyzed using the Rietveld analysis program RIETAN2000 [A], providing detailed information about the crystal structure. Steady-state absorption spectra were acquired using a JASCO V-670 spectrophotometer. To examine lattice vibrations, Raman spectroscopy was performed with a JASCO NRS4500 NMDS instrument, employing a 532 nm excitation (green) laser. X-ray photoelectron spectroscopy (XPS) was carried out using a JEOL JPS-9030 instrument, utilizing an X-ray source of Mg K Alfa (monochromatic) with a 25 mA beam current and 12 kV. This technique provided valuable information about the elemental composition and chemical states of the samples.

Table 1 Molar ratios of raw materials used for iron-doped $Cs_3Bi_2Br_9$ perovskite

CsBr (mmol)	$BiBr_3$ (mmol)	$FeBr_3$ (mmol)	Alloying composition (%)
3	2	w/0	0%
3	1.9	0.1	5%
3	1.6	0.4	20%
3	1	1	50%
3	0.6	1.4	70%
3	w/0	2	100%

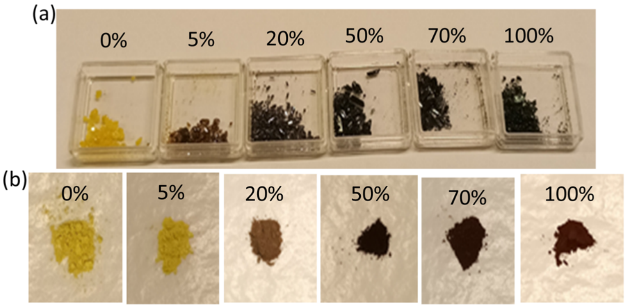

Fig. 1 (a) Photographs of perovskite crystals with varying Fe alloying concentrations. The images showcase the color transition of the crystals, ranging from yellow to darker shades as the Fe concentration increases, underscoring the notable color tunability of the perovskite materials in response to different Fe concentrations. (b) Photographs of powdered perovskite materials after grinding the crystals. The ground powders exhibit the resultant color change, emphasizing the impact of Fe doping on the optical properties of the perovskite materials.

Results and discussion

The $Cs_3Bi_2Br_9$ perovskite crystals with varying Fe concentrations (0, 5, 20, 50, 70, and 100 at%) exhibit a distinct color transition from yellow to a darker shade, as depicted in Fig. 1(a). This color tunability strongly implies variations in bandgap energy and material replacement among these materials.[23] Upon grinding the crystals, the materials exhibit a darker coloration at higher Fe doping concentrations, as illustrated in Fig. 1(b). It suggests that Fe^{3+} can be fully substituted for Bi^{3+} in $Cs_3Bi_2Br_9$.

As shown in Fig. 1(b), the color of the doped material darkens with increasing Fe concentration, suggesting a variation in bandgap energy. This visual correlation is further supported by the UV-vis absorption spectroscopy presented in Fig. 2(a). The adsorption edge of the undoped material, observed around 430 nm, aligns with previous reports.[22] As the concentration of Fe increases, the optical absorbance band edge of the doping materials also increases, reaching approximately 490 nm. The UV-vis spectra exhibit three distinct types of curves corresponding to different doping concentrations, each characterized by a unique crystal structure. The optical bandgap of the materials is estimated from UV spectra using Tauc plots of $(\alpha h\nu)^n$ *versus* $h\nu$. The $Cs_3Bi_2Br_9$ perovskite possesses both direct and indirect bandgaps.[39,45] The indirect bandgap values of the pristine and doped $Cs_3Bi_2Br_9$ are 2.54 eV, 2.53 eV, 2.39 eV, 1.80 eV, 1.78 eV, and 1.88 eV, and the corresponding direct bandgap values are 2.69 eV, 2.67 eV, 2.61 eV, 1.99 eV, 1.97 eV, and 2.17 eV for 0%, 5%, 20%, 50%, 70%, and 100% Fe doping, respectively as shown in Fig. 2(b) and (c). The bandgap value of the pristine $Cs_3Bi_2Br_9$ perovskite material is in good agreement with previous reports.[40,46] These tunable optical bandgap energies align with the observed color changes in different Fe doping concentrations. Both the direct and indirect bandgaps shift towards lower values with increasing Fe content compared to the pristine $Cs_3Bi_2Br_9$ perovskite. The indirect bandgap values are consistently smaller than the direct bandgap values,

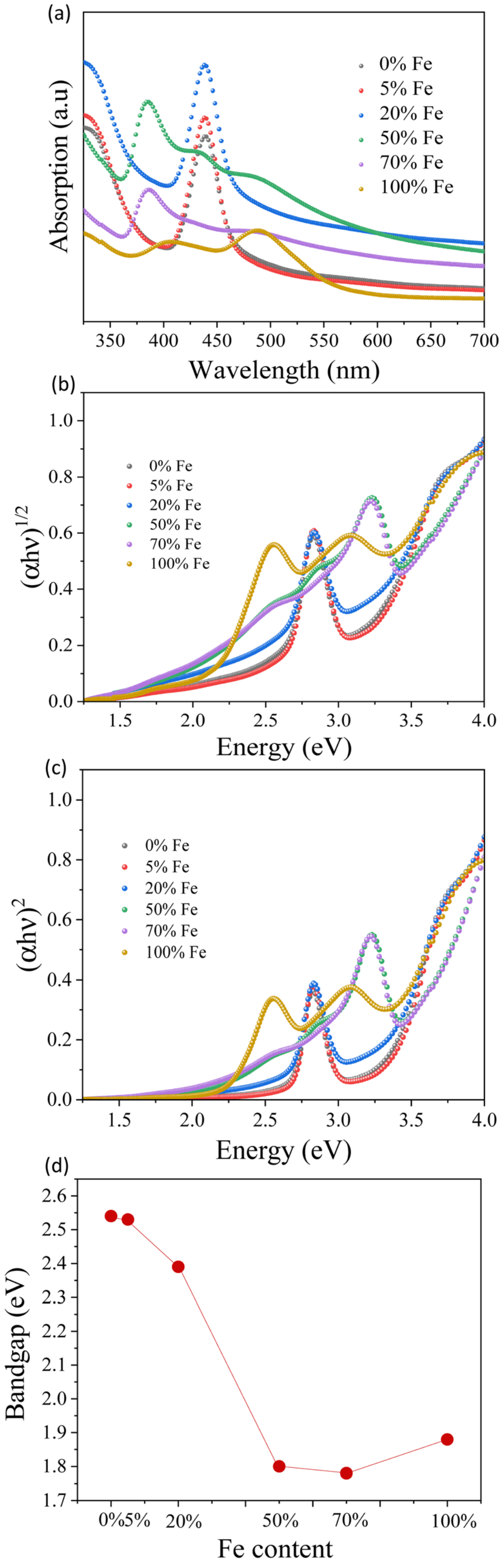

Fig. 2 (a) UV-Vis absorption spectra, Tauc plots of (b) indirect bandgap and (c) direct bandgap, and (d) indirect bandgap energies of different Fe doping materials.

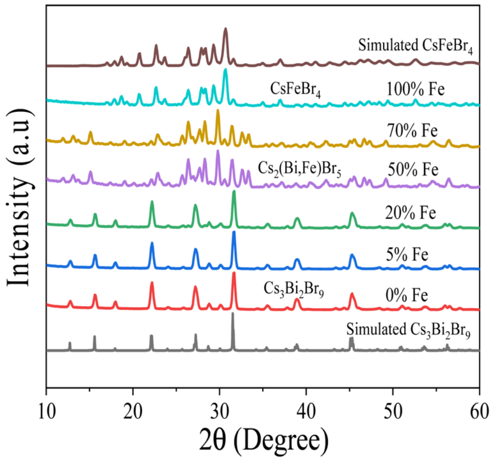

Fig. 3 XRD patterns of $Cs_3Bi_2Br_9$ with different doping concentrations.

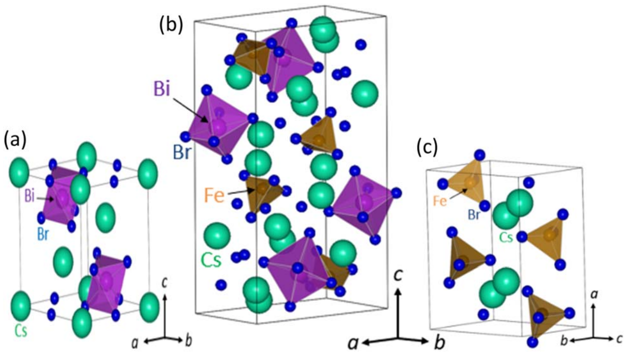

Fig. 4 Crystal structure of (a) $Cs_3Bi_2Br_9$ (b) $Cs_2(Bi,Fe)Br_5$ and (c) $CsFeBr_4$.

although the trend is the same for both methods of calculation. The PL peak does not appear when we measure the Raman spectroscopy as illustrated in ESI Fig. S1.† Therefore, we assume that both the pristine and doped $Cs_3Bi_2Br_9$ perovskite have an indirect bandgap. The indirect bandgap energies exhibit a gradual decrease, ranging from 2.54 eV to 2.39 eV for the 0%, 5%, and 20% compositions of the perovskite material characterized by the $Cs_3Bi_2Br_9$ perovskite structure. For the $Cs_2(Bi,Fe)Br_5$ perovskite material, the bandgap energies shift from 1.80 eV to 1.78 eV in the case of the 50% and 70% Fe doping. Notably, 70% Fe doping stands out with the lowest bandgap energy of 1.78 eV, as shown in Fig. 2(d). The bandgap energy for the $CsFeBr_4$ structure with 100% Fe occupancy is measured at 1.88 eV. This tunability in bandgap energy holds promise for applications that require tailored optical properties, emphasizing the influence on optoelectronic devices.

There is a possibility that variation in bandgap from 2.69 eV to 1.97 eV could be associated with crystal structure change due to Fe doping. Therefore, we further examined the crystal structure of the perovskites at various Fe doping using XRD and Rietveld analysis. Fig. 3 shows the XRD pattern of Fe-doped $Cs_3Bi_2Br_9$ perovskite for concentrations ranging from 0% to 100% Fe. The powder XRD measurements of the pristine, 5% Fe-, and 20% Fe-doped perovskites are in agreement with the $Cs_3Bi_2Br_9$ trigonal crystal structure illustrated in Fig. 4(a), maintaining the space group *P*3m1 as previously reported in the literature.[23] The structural parameters were refined using Rietveld analysis of XRD data, based on the structural model as shown in in ESI Fig. S2.† The XRD patterns of the pristine, 5%, and 20% Fe-doped samples were consistent with the $Cs_3Bi_2Br_9$ structure as depicted in ESI Fig. S2(a)–(c).† Notably, both the *a* and *c* axes increased with higher Fe doping levels, suggesting the substitution of Fe atoms into the Bi site. Additionally, a structural transformation becomes evident at 50% Fe doping, where the diffraction patterns show an orthorhombic structure characteristic of $Cs_2(Bi,Fe)Br_5$ perovskite with a space group *Pnma*, as illustrated in Fig. 4(b). This crystal structure has two metal-occupied sites, namely octahedral and tetrahedral sites. Consequently, we conducted Rietveld analysis on two models: one with Bi occupying an octahedral site and Fe occupying a tetrahedral site, and the other with Bi occupying a tetrahedral site and Fe occupying an octahedral site. When the Bi atoms occupied octahedral sites, the resulting reliability factor was $R_{wp} = 6.33\%$ as illustrated in ESI Fig. S2(d).† On the other hand, Bi atoms occupied at tetrahedral sites, the R_{wp} becomes worse from 6.33% to 12.85%. This outcome indicates that Bi atoms occupied octahedral sites and Fe atoms occupy tetrahedral sites. The diffraction pattern of the 70% Fe alloy sample could be indexed by the $Cs_2(Bi,Fe)Br_5$ structure, with lattice constants increasing with Fe doping. This tendency is similar to that of Fe doping in $Cs_3Bi_2Br_9$, suggesting a substitution of Fe in the pristine material *via* the orthorhombic structure.[23] For the 100% Fe alloying material, all diffraction peaks correspond to the orthorhombic structure of $CsFeBr_4$ perovskite, characterized by the space group *Pnma*, presented in Fig. 4(c). The resulting reliability factor from the Rietveld refinement was $R_{wp} = 4.04\%$, as shown in ESI Fig. S2(f).† Interestingly, in $CsFeBr_4$, Fe ions exhibit tetrahedral coordination, suggesting that the structural

Table 2 Energy dispersive spectroscopy (EDS) data for alloying composition of all elements

Cs (at%)	Fe (at%)	Bi (at%)	Br (at%)	Estimated structure	Alloying composition (%)
20.97	w/0	12.85	66.17	$A_3B_2X_9$	0%
24.85	1.61	11.91	61.63	$A_3B_2X_9$	5%
23.32	4.88	7.08	64.71	$A_3B_2X_9$	20%
25.41	6.45	6.38	61.76	A_2BX_5	50%
24.03	6.81	4.37	64.79	A_2BX_5	70%
15.16	16.99	w/0	67.85	ABX_4	100%

change induced by Fe doping is associated with the preferential tetrahedral coordination of Fe. This leads to the presence of a tertiary phase ($CsFeBr_4$) in the $Cs_3Bi_2Br_9$ perovskite at 100% Fe alloying. From the XPD analysis, we postulate that the transformation of crystal structure from $Cs_3Bi_2Br_9$ to $Cs_2(Bi,Fe)Br_5$ and $CsFeBr_4$ at higher Fe doping may also contribute to significant bandgap change in the perovskites.

The elemental composition of the perovskite crystals was scrutinized using energy dispersive spectroscopy (EDS), and the alloying composition of all elements (Cs, Bi, Fe, and Br) is detailed in Table 2. Analysis reveals a correlation between the precursor and product compositions, indicating a preference for the incorporation of Fe into the pristine perovskite material. The EDS results further enable an estimation of the crystal structures. The $A_3B_2X_9$ perovskite structure is observed for 0%, 5%, and 20% Fe doping, while the A_2BX_5 perovskite structure is identified for 50% and 70% Fe doping. Interestingly, the 100% Fe doping results in the ABX_4 perovskite structure. These findings align with the XRD measurements, where the $Cs_3Bi_2Br_9$ structure is retained for 0%, 5%, and 20% Fe doping, $Cs_2(Bi,Fe)Br_5$ structure emerges for 50% and 70% Fe doping, and $CsFeBr_4$ structure is observed for 100% Fe doping. The comprehensive characterization sheds light on the structural transformations induced by varying Fe concentrations in the perovskite crystals. Energy dispersive spectroscopy (EDS) elemental mapping,

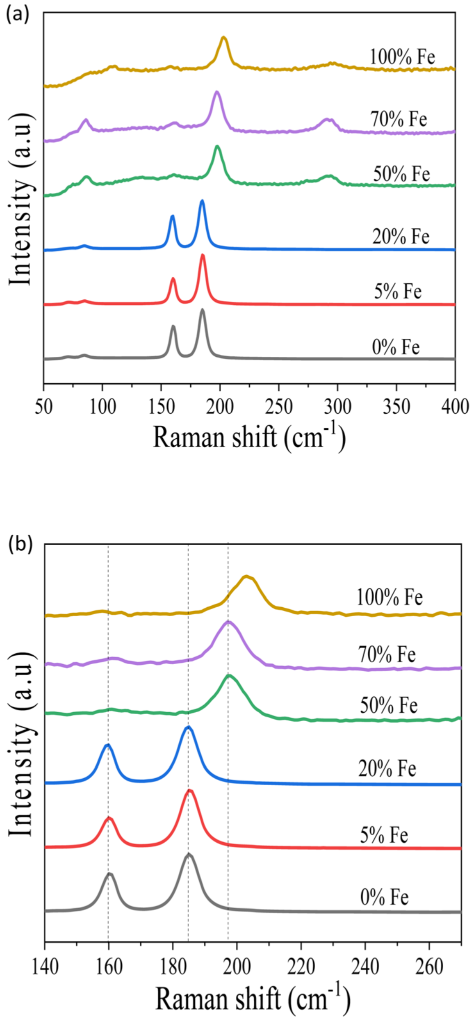

Fig. 5 (a) Raman spectra of the pristine $Cs_3Bi_2Br_9$ and Fe doped perovskite crystals. (b) Expansion of Raman spectra.

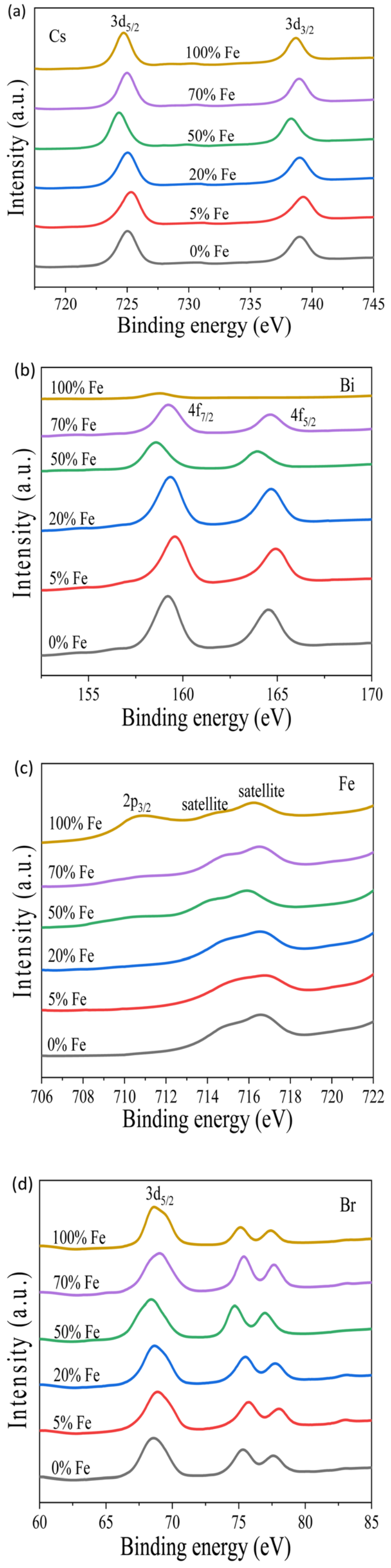

Fig. 6 XPS Spectra of (a) Cs 3d, (b) Bi 4f, (c) Fe 2p and (d) Br 3d.

shown in ESI Fig. S3,† demonstrates the same magnitude for all compositions. Despite some mappings being less clear, the overall tendency indicates a homogeneous decrease of Bi and an increase of Fe with increasing Fe content.

To verify the structural origin and phase purity of the pristine and alloyed perovskites, Raman spectra were obtained, as shown in Fig. 5(a). The peaks of undoped materials at 160 cm^{-1} and 187 cm^{-1} are attributed to the stretching vibrations of the Bi–Br bond with E_g and A_{1g} symmetry in $BiBr_6$ octahedra, respectively, which are vibrations with participation of Bi atoms. These results correspond well with prior reports.[47,48] The absence of shifts in peak positions and intensity changes upon 20% or lower Fe doping suggests that Fe incorporation does not affect the crystal structure of the pristine material. New vibration mode at around 200 cm^{-1} appears from 50% to 100% alloyed materials, attributed to the stretching modes of Fe–Br bonds,[49] absent in the parent $Cs_3Bi_2Br_9$ material. The Raman peak at around 200 cm^{-1} broadens and shifts toward higher wavenumbers with 70% Fe and greater, as shown in Fig. 5(b), due to different ionic radius of the doping metal, Fe^{3+} (63 pm) and parent metal Bi^{3+}(103 pm). This also indicates the substitution of Bi^{3+} with Fe^{3+} in the crystal structure.[40]

To investigate the incorporation of Fe into the pristine material, X-ray photoelectron spectroscopy (XPS) was utilized, revealing core levels of Cs 3d, Bi 4f, Br 3d, and an additional element, Fe, as depicted in Fig. 6. The Cs $3d_{5/2}$ and Cs $3d_{3/2}$ binding energies at 724 eV and 738 eV, respectively, align with previous reports.[39] The Br $3d_{5/2}$ peak is located at 68 eV. Fig. 6(b) shows Bi exhibits doublet peaks corresponding to $4f_{7/2}$ at 159.3 eV and $4f_{5/2}$ at 164.6 eV, which matches with the previous results.[41] At 100% Fe doping, the disappearance of these doublets is a result of the complete occupation by Fe. The binding energy of Bi 4f at 160 eV observed at 100% Fe doping is the spectral line from the $4p_{3/2}$ peak of Cs. The Fe $2p_{3/2}$ peak at 711 eV at 100% Fe doping confirms the successful doping of Fe into the pristine perovskite material as presented in Fig. 6(c). The consistency of this outcome aligns with other characterization results, including XRD and EDS analyses. Consequently, we have successfully doped Fe into the pristine $Cs_3Bi_2Br_9$ perovskite material, leading to a potential reduction in its bandgap for optoelectronic applications.

Conclusions

In conclusion, the synthesis of nontoxic lead-free $Cs_3Bi_2Br_9$ perovskite material with varying Fe doping concentrations has been successfully achieved through a facile method. The investigation of the structural and optical properties of Fe-doped Bi-based material has provided valuable insights. The pristine $Cs_3Bi_2Br_9$ crystal structure maintains its trigonal crystal structure with space group $P\bar{3}m1$. However, a secondary phase transformation to $Cs_2(Bi,Fe)Br_5$ is observed with 50% Fe doping, and successful Fe incorporation into the pristine perovskite ($Cs_3Bi_2Br_9$) results in the formation of the orthorhombic crystal structure $CsFeBr_4$ perovskite. Notably, the bandgap of the material undergoes a reduction from 2.54 eV for the pristine to 1.78 eV with 70% Fe alloying. This tunability in bandgap energy holds significant implications for potential applications in optoelectronic devices, highlighting the suitability of Fe-doped $Cs_3Bi_2Br_9$ perovskite crystals for environmentally friendly, lead-free perovskite-based optoelectronic applications. This work represents a crucial step forward in the exploration and utilization of lead-free perovskite materials in the field of optoelectronics.

Conflicts of interest

The authors declare that they have no conflict of interest.

Acknowledgements

The author gratefully acknowledges financial support from the Ministry of Education, Culture, Sports, Science and Technology (MEXT) of Japan for PhD scholarship.

References

1 B.-W. Park, B. Philippe, X. Zhang, H. Rensmo, G. Boschloo and E. M. J. Johansson, *Adv. Mater.*, 2015, **27**, 6806–6813.
2 B. Yang, J. Chen, F. Hong, X. Mao, K. Zheng, S. Yang, Y. Li, T. Pullerits, W. Deng and K. Han, *Angew. Chem., Int. Ed.*, 2017, **56**, 12471–12475.
3 F. H. Gourji and D. Velauthapillai, *Molecules*, 2021, **26**, 1–45.
4 Z.-K. Tang, Z.-F. Xu, D.-Y. Zhang, S.-X. Hu, W.-M. Lau and L.-M. Liu, *Sci. Rep.*, 2017, **7**, 1–7.
5 J. H Heo and S. H. Im, *Adv. Mater.*, 2016, **28**, 5121–5125.
6 H.-M. Huang, Z.-Y. Jiang, Y.-M. Lin, B. Zhou and C.-K. Zhang, *Appl. Phys. Express*, 2017, **10**, 123002.
7 D. Shen, X. Wang, X. Zhang, Y. Liu, Y. Shi, X. Li, X. Chen and Y. Zhang, *ACS Appl. Opt. Mater.*, 2022, **1**, 435–441.
8 S. Ghosh, S. S. Mukhopadhyay, S. Paul, B. Pradhan and S. K. De, *ACS Appl. Nano Mater.*, 2020, **3**, 11107–11117.
9 C. Liu, L. Wang, F. Fang, Z. Zhao, J. Pan, J. Akram, S. Shafie, R. Tala-Ighil, Q. Li, Z. Zhao, J. Wu, Z. Zhu, W. Lei, X. Zhang and J. Chen, *Front. Mater.*, 2021, **8**, 682833.
10 A. K. Baranwal, H. Masutani, H. Sugita, H. Kanda, S. Kanaya, N. Shibayama, Y. Sanehira, M. Ikegami, Y. Numata, K. Yamada, T. Miyasaka, T. Umeyama, H. Imahori and S. Ito, *Nano Converg.*, 2017, **4**, 1–14.
11 M. Usman and Q. Yan, *Crystals*, 2020, **10**, 62.
12 X. Li, X. Du, P. Zhang, Y. Hua, L. Liu, G. Niu, G. Zhang, J. Tang and X. Tao, *Sci. China Mater.*, 2021, **64**, 1427–1436.
13 Z. Jin, Z. Zhang, J. Xiu, H. Song, T. Gatti and Z. He, *J. Mater. Chem. A*, 2020, **8**, 16166–16188.
14 L. Romani, A. Speltini, C. N. Dibenedetto, A. Listorti, F. Ambrosio, E. Mosconi, A. Simbula, M. Saba, A. Profumo, P. Quadrelli, F. De Angelis and L. Malavasi, *Adv. Funct. Mater.*, 2021, **31**, 2104428.
15 F. Wei, F. Brivio, Y. Wu, S. Sun, P. D. Bristowe and A. K. Cheetham, *J. Mater. Chem. C*, 2018, **6**, 3573–3577.
16 S. Sun, N. T. P. Hartono, Z. Ren, F. Oviedo, A. M. Buscemi, M. Layurova, D. X. Chen, T. Ogunfunmi, J. Thapa, S. Ramasamy, C. Settens, B. L. DeCost, A. G. Kusne, Z. Liu,

S. I. P. Tian, I. M. Peters, J.-P. Correa-Baena and T. Buonassisi, *Joule*, 2019, **3**, 1437–1451.
17 M. T. Sirtl, R. Hooijer, M. Armer, F. G. Ebadi, M. Mohammadi, C. Maheu, A. Weis, B. V. van Gorkom, S. Häringer, R. A. J. Janssen, T. Mayer, V. Dyakonov, W. Tress and T. Bein, *Adv. Energy Mater.*, 2022, **12**, 2103215.
18 O. Akinbami, R. Moepya, G. N. Ngubeni, P. Tetyana, K. P. Mubiayi, M. J. Moloto and N. Moloto, *J. Photochem. Photobiol. Chem.*, 2021, **419**, 113460.
19 J.-P. Correa-Baena, L. Nienhaus, R. C. Kurchin, S. S. Shin, S. Wieghold, N. T. P. Hartono, M. Layurova, N. D. Klein, J. R. Poindexter, A. Polizzotti, S. Sun, M. G. Bawendi and T. Buonassisi, *Chem. Mater.*, 2018, **30**, 3734–3742.
20 J.-Y. Gu, G. Yan, Y. Lian, Q. Mu, H. Jin, Z. Zhang, Z. Deng and Y. Peng, *RSC Adv.*, 2018, **8**, 25802–25807.
21 S.-Y. Kim, Y. Yun, S. Shin, J.-H. Lee, Y.-W. Heo and S. Lee, *Scr. Mater.*, 2019, **166**, 107–111.
22 C. J. Krajewska, S. R. Kavanagh, L. Zhang, D. J. Kubicki, K. Dey, K. Galkowski, C. P. Grey, S. D. Stranks, A. Walsh, D. O. Scanlon and R. G. Palgrave, *Chem. Sci.*, 2021, **12**, 14686–14699.
23 A. Elattar, L. Kobera, J. Kangsabanik, H. Suzuki, S. Abbrent, T. Nishikawa, K. S. Thygesen, J. Brus and Y. Hayashi, *J. Mater. Chem. C*, 2022, **10**, 12863–12872.
24 N. K. Tailor, S. Mishra, T. Sharma, A. K. De and S. Satapathi, *J. Phys. Chem. C*, 2021, **125**, 9891–9898.
25 A. J. Lehner, D. H. Fabini, H. A. Evans, C.-A. Hébert, S. R. Smock, J. Hu, H. Wang, J. W. Zwanziger, M. L. Chabinyc and R. Seshadri, *Chem. Mater.*, 2015, **27**, 7137–7148.
26 H. X. Zhu, X. H. Wang and G. C. Zhuang, *Appl. Phys. A*, 2019, **125**, 1–10.
27 Z. Zhang, L. Ren, H. Yan, S. Guo, S. Wang, M. Wang and K. Jin, *J. Phys. Chem. C*, 2017, **121**, 17436–17441.
28 L. Zhang, K. Wang and B. Zou, *ChemSusChem*, 2019, **12**, 1612–1630.
29 Z. Tan, J. Li, C. Zhang, Z. Li, Q. Hu, Z. Xiao, T. Kamiya, H. Hosono, G. Niu, E. Lifshitz, Y. Cheng and J. Tang, *Adv. Funct. Mater.*, 2018, **28**, 1801131.
30 N. Ding, D. Zhou, G. Pan, W. Xu, X. Chen, D. Li, X. Zhang, J. Zhu, Y. Ji and H. Song, *ACS Sustain. Chem. Eng.*, 2019, **7**, 8397–8404.
31 C. Zuo and L. Ding, *Angew. Chem., Int. Ed.*, 2017, **56**, 6528–6532.
32 S. Ghosh and B. Pradhan, *ChemNanoMat*, 2019, **5**, 300–312.
33 M. Shi, B. Yang, S. Liu, R. Zhang, K. Han, C. Li and R. Li, *Energy Mater. Adv.*, 2022, **2022**, 1–11.
34 Z. Ji, Y. Liu, W. Li, C. Zhao and W. Mai, *Sci. Bull.*, 2020, **65**, 1371–1379.
35 M. T. Kovsarnechan, J. Roziere, D. Mascherpa-Corral and I. inotg, *Nucl. Chem.*, 1978, **40**, 2009–2011.
36 S. Wieghold, A. S. Bieber, M. Mardani, T. Siegrist and L. Nienhaus, *J. Mater. Chem. C*, 2020, **8**, 9714.
37 S. Tang, S. Huang, G. J. Wilson and A. Ho-Baillie, *Trends Chem.*, 2020, **2**, 638–653.
38 S. Dai, X. Gan, K. Li, Q. Huang, L. Guo and H. Liu, *Phys. Chem. Chem. Phys.*, 2023, **25**, 30993.
39 M. Roy, S. Ghorui, Bhawna, J. Kangsabanik, R. Yadav, A. Alam and M. Aslam, *J. Phys. Chem. C*, 2020, **124**, 19484–19491.
40 M. N. Tran, I. J. Cleveland, G. A. Pustorino and E. S. Aydil, *J. Mater. Chem. A*, 2021, **9**, 13026.
41 X. Cheng, L. Jing, Y. Yuan, S. Du, J. Zhang, X. Zhan, J. Ding, H. Yu and G. Shi, *J. Phys. Chem. C*, 2019, **123**, 1669–1676.
42 G. Jayanthi, S. Sumathi, K. Kannan, V. Andal and S. Murugan, *Adv. Mater. Sci. Eng.*, 2022, **2022**, 1–14.
43 Y. Hu, X. Zhang, C. Yang, J. Li and L. Wang, *RSC Adv.*, 2019, **9**, 33017–33022.
44 N. Li, Q. Zhang and W. Yang, *Appl. Phys. Lett.*, 2020, **117**, 080502.
45 Y. Zhang, J. Yin, M. R. Parida, G. H. Ahmed, J. Pan, O. M. Bakr, J.-L. Brédas and O. F. Mohammed, *J. Phys. Chem. Lett.*, 2017, **8**, 3173–3177.
46 K. K. Bass, L. Estergreen, C. N. Savory, J. Buckeridge, D. O. Scanlon, P. I. Djurovich, S. E. Bradforth, M. E. Thompson and B. C. Melot, *Inorg. Chem.*, 2017, **56**, 42–45.
47 G. Bator, J. Baran, R. Jakubas and M. Karbowiak, *Vib. Spectrosc.*, 1998, **16**, 11–20.
48 M. Y. Valakh, M. P. Lisitsa, E. Y. Peresh, O. V. Trylis and A. M. Yaremko, *J. Mol. Struct.*, 1997, **436–437**, 309–313.
49 A. García-Saiz, I. de Pedro, P. Migowski, O. Vallcorba, J. Junquera, J. A. Blanco, O. Fabelo, D. Sheptyakov, J. C. Waerenborgh, M. T. Fernández-Díaz, J. Rius, J. Dupont, J. A. Gonzalez and J. R. Fernández, *Inorg. Chem.*, 2014, **53**, 8384–8396.